Infrared Physics & Technology 151 (2025) 106071

Contents lists available at ScienceDirect

Infrared Physics and Technology

journal homepage: www.elsevier.com/locate/infrared

Research Paper

Cantilever-amplified spindle bubble microcavity for high-sensitivity and robust fiber-optic strain sensing

Jianxin Wang [a], Weiqiang Wang [a], Jingwei Lv [a], Famei Wang [b], Wei Liu [a], Zao Yi [c], Qiang Liu [a], Paul K. Chu [d], Chao Liu [a,*]

[a] School of Physics and Electronic Engineering, Northeast Petroleum University, Daqing 163318, China
[b] Shenzhen Key Laboratory of Ultra-Intense Laser and Advanced Material Technology, Center for Intense Laser Application Technology, and College of Engineering Physics, Shenzhen Technology University, Shenzhen 518118, China
[c] Joint Laboratory for Extreme Conditions Matter Properties, Southwest University of Science and Technology, Mianyang 621010, China
[d] Department of Physics, Department of Materials Science and Engineering, and Department of Biomedical Engineering, City University of Hong Kong, Tat Chee Avenue, Kowloon, Hong Kong, China

ARTICLE INFO

Keywords:
Fabry-Pérot interferometer
Fiber micro-shaping
Spindle-shaped bubble
Flexible wearables

ABSTRACT

Fiber-optic Fabry-Pérot interferometric (FPI) sensors based on bubble microcavities are fundamentally limited by the sensitivity-robustness trade-off. To overcome this, we propose a spindle-shaped bubble geometry with a cladding-protruding long axis, fabricated via an improved fiber micro-shaping technique using only a commercial fusion splicer. Through parametric optimization guided by experiments and finite element simulations, we demonstrate that the protruding axis acts as a cantilever amplifier, converting axial strain (short-axis direction) into amplified displacement at the long-axis free end, thereby enhancing cavity-length modulation efficiency by 86 %. The optimized structure achieves 49.65 pm/με strain sensitivity at 1,550 nm while withstanding bending radii $\leq$ 2.5 cm—surpassing Fully-embedded bubble FPIs by 32.1 % in tensile resistance and 36.2 % in bending tolerance. This innovation bridges the gap between high sensitivity and mechanical robustness, making it ideal for flexible wearables or complex wiring scenarios.

1. Introduction

Optical fiber sensors have attracted significant interest in sensing applications due to their unique advantages such as high sensitivity, corrosion resistance, and compact structure, boding well for the monitoring of physical parameters such as refractive indexes [1–3], magnetic fields [4–6], and temperature [7–9]. In particular, optical fiber FPIs based on air microcavities are promising in strain sensing on account of their simple structure, high sensitivity, compact size, and low temperature cross-sensitivity [10–12]. However, existing bubble-based FPI sensors face an inherent trade-off between sensitivity and mechanical reliability: enhancing sensitivity typically requires reducing microcavity dimensions or wall thickness, which inevitably compromises structural durability under tensile/bending loads [13,14]. Recent efforts to optimize strain-transfer mechanisms remain limited by fundamental fabrication constraints.

To improve the strain sensitivity for high-resolution microstrain detection, efforts have been made to tailor the air-cavity geometries. In 2014, Liu et al. first demonstrated a low-cost FPI fabrication method by embedding an air microcavity in the SMF using a commercial fusion splicer [15]. While they observed that shorter cavity lengths improved sensitivity, this approach could only produce thicker-walled FPIs and lacked in-depth analysis of bubble structures. Later that same year, Yin et al. proposed an inflated bubble microcavity structure with a protruding long axis [16], which achieved higher sensitivity while maintaining moderate mechanical strength (withstanding strains below 1,300 με). Subsequently, similar approaches were developed, yet these methods invariably required hazardous Hydrofluoric acid (HF) etching [11,17]. In 2015, Liu et al. optimized the fabrication process to create rectangular air bubbles, enhancing sensitivity through wall thickness reduction but sacrificing mechanical durability [13]. Subsequently, alternative approaches emerged, such as using multimode fibers or quartz capillaries to create expanded spherical bubbles for high-sensitivity FPIs [18–20]. In 2021, Yin et al. employed femtosecond-laser-etched concave grooves on tapered fiber ends to form protruding bubble cavities while investigating shape-dependent performance [14].

* Corresponding author.
E-mail address: msm-liu@126.com (C. Liu).

https://doi.org/10.1016/j.infrared.2025.106071
Received 21 June 2025; Received in revised form 8 August 2025; Accepted 11 August 2025
Available online 12 August 2025

Critically, this method suffered from poor structural controllability, and the resulting sensors fractured below 240 με, rendering them impractical. To date, simultaneously achieving both high sensitivity and robust mechanical properties remains a critical challenge for bubble-based FPIs.

Herein, an improved fiber micro-shaping technique is described to fabricate a spindle-shaped bubble microcavity with a cladding-protruding long axis using only a commercial fusion splicer. The spindle-shaped cavity exhibits a tapered geometry (narrow ends and a wide center) in the axial cross-section, with the long axis protruding beyond the cladding to create a stress-engineered cantilever-like amplification system. While recent advances exploit cascaded bubbles for biomedical sensing [21] or Vernier-effect FPIs for ultra-high sensitivity [22,23], these approaches face inherent complexity in fabrication/alignment and neglect mechanical durability. In contrast, our spindle-shaped bubble sensor introduces a cantilever-driven strain amplification mechanism, unifying high sensitivity (49.65 pm/με) with exceptional resilience to bending (radius ≤ 2.5 cm) and strain (>960 με). Compared to Fully-embedded bubble FPIs with similar sensitivity, our device exhibits 32.1 % higher tensile resistance and 36.2 % superior bending tolerance, enabling reliable operation in flexible wearables or complex wiring scenarios and bridging the gap between sensitivity and robustness.

2. Principles and device fabrication

Fig. 1 shows the schematic of the spindle-shaped bubble microcavity fiber sensor. The spindle-shaped bubble microcavity, when observed from the axial cross-section of the fiber, has a tapered geometry with narrow ends and a wide center, while its long axis protrudes beyond the fiber cladding. The protruding long axis functions as a cantilever beam with its fixed end at the cladding interface and free end at the bubble vertex. As illustrated in Fig. 1(a), the yellow dashed line represents the fiber axis, L_{minor} denotes the cavity length of the spindle-shaped bubble, D_1 and D_2 are the cladding diameters at the bubble edges, with an average diameter defined as $D_{avg} = (D_1 + D_2)/2$, t_1 and t_2 correspond to the minimum residual cladding widths on the upper and lower sides of the bubble, respectively, with an average width $t_{avg} = (t_1 + t_2)/2$, D_m represents the maximum cladding length within the bubble region, and its variation under tensile strain is defined as Δd. The height difference of the spindle-shaped cladding is defined as $\Delta h = D_m\text{-}D_{avg}$, $(\Delta h > 0)$. In contrast, fully-embedded bubble structures refer to microbubbles completely confined within the fiber cladding ($\Delta h \leq 0$).

When light impinges on the air cavity, it is partially reflected at the glass-air interface, while the transmitted light propagates into the cavity. The transmitted light is then reflected back into the core at the air-glass interface to interfere with the forward-reflected light. Owing to the low reflectivity (<4%) of the non-flat surfaces, multiple reflections can be neglected [24]. As a result, the interference spectrum can be analyzed

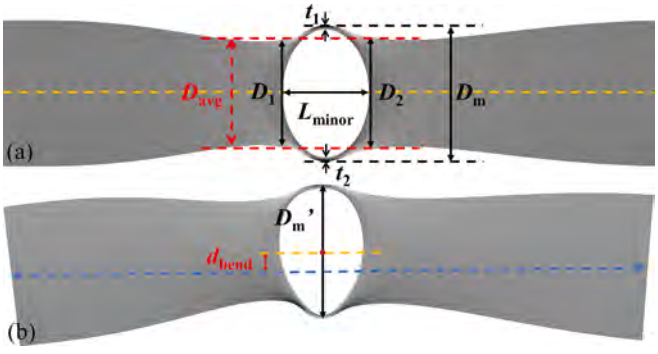

Fig. 1. Schematic diagram of the sensor: (a) Straight/unconstrained optical fiber sensor and (b) Bent optical fiber sensor.

using the two-beam interference model [25]:

$$I_S = I_1 + I_2 + 2\sqrt{I_1 I_2}COS(\theta) \quad (1)$$

where I_1 and I_2 are the intensities reflected from the two cavity interfaces and θ denotes the initial phase. The Free Spectral Range (**FSR**), i.e., the wavelength interval between two adjacent resonant peaks, is shown in the following [14,26]:

$$\mathrm{FSR} = \lambda(m+1) - \lambda(m) = \frac{\lambda(m+1)\lambda(m)}{2n_{eff}L_{\mathrm{minor}}} \quad (2)$$

where m is the interference order, $\lambda(m)$ is the resonant wavelength corresponding to the m-**th** order, and n_{eff} is the refractive index of air. When strain is applied, the refractive index n_{eff} remains constant, while the cavity length L_{minor} increases by ΔL, causing $\lambda(m)$ to shift toward longer wavelengths (redshift).

As shown in Fig. 1(b), D_m' represents the state of the original variable D_m after bending, and the blue dashed line corresponds to the chord of the bent fiber axis. The vertical distance between this chord and the original axis is defined as d_{bend}, which quantifies the bending degree. To evaluate the tensile and bending resistance of bubble microcavities with different geometries, we define the maximum stress (σ_{max}) and maximum deformation (u_{max}) at the edges or vulnerable regions of the microcavity under tensile or bending conditions. A comprehensive performance factor $F = \Delta L/|u_{max}|$ is introduced, where ΔL is the cavity length change. The physical meaning of F is the cavity length variation per unit maximum deformation. For bubble microcavity sensors with different structures, a larger F indicates greater deformation conversion efficiency. That is, for the same $|u_{max}|$, a larger ΔL is achieved.

Fig. 2 illustrates the fabrication process of the spindle-shaped bubble in the SMF (Corning SMF-28), utilizing a fusion splicer (Fujikura 80S; note: the "bit" unit for the discharge power is a relative calibration value internal to the device and positively correlated with the discharge intensity) and index-matching gel (Cargille Labs, https://www.cargille.com). The process comprises six steps:

In **Step 1** [Fig. 2(I)], two SMF segments are placed in the left and right fiber holders of the splicer. Their ends are smoothed by arc discharge (discharge power: −5 bit, duration: 800 ms).

In **Step 2** [Fig. 2(II)], the motor-driven stage advances the fiber (precoated with index-matching gel at its tip) to contact the opposing fiber under preload compression, followed by arc discharge (−5 bit, 800 ms) to form a microscale bubble cavity.

In **Step 3** [Fig. 2(III)], the motor remains stationary, and discharge parameters are adjusted (+15 bit, 1800 ms) to expand the bubble in a single discharge cycle.

In **Step 4** [Fig. 2(IV)], the bubble center is slightly offset from the discharge zone. Preload tension is applied, and repeated discharges (+15 bit, 1800 ms) are performed until the bubble diameter exceeds the fiber diameter at the discharge center.

Step 5 [Fig. 2(V)] mirrors **Step 4** but shifts the bubble center to the opposite side of the discharge zone, followed by tension and repeated discharges (+15 bit, 1800 ms) to further enlarge the bubble.

In **Step 6** [Fig. 2(VI)], the bubble is recentered, and a final preload compression with discharge (−5 bit, 300 ms) completes the spindle-shaped bubble microcavity.

Manufacturing precision and yield were critical for parametric optimization. Cavity length (L_{minor}) was controlled within ± 1 μm via iterative discharges (Fig. 2(VI)), while wall thickness (t_{avg}) maintained 3–5 μm through real-time arc power adjustment. Batch testing (25 devices) showed > 80 % yield for sensors with sensitivity > 30 pm/με, though stochastic plasma variations prevented identical bubble replication.

Fig. 3 displays the microscopic images (Olympus CX31, **40** × magnification) of the fabricated spindle-shaped bubble microcavity sensor, which is analyzed by the cellSens Entry software. As shown in Fig. 3(a), the microcavity embedded in the SMF has a spindle geometry

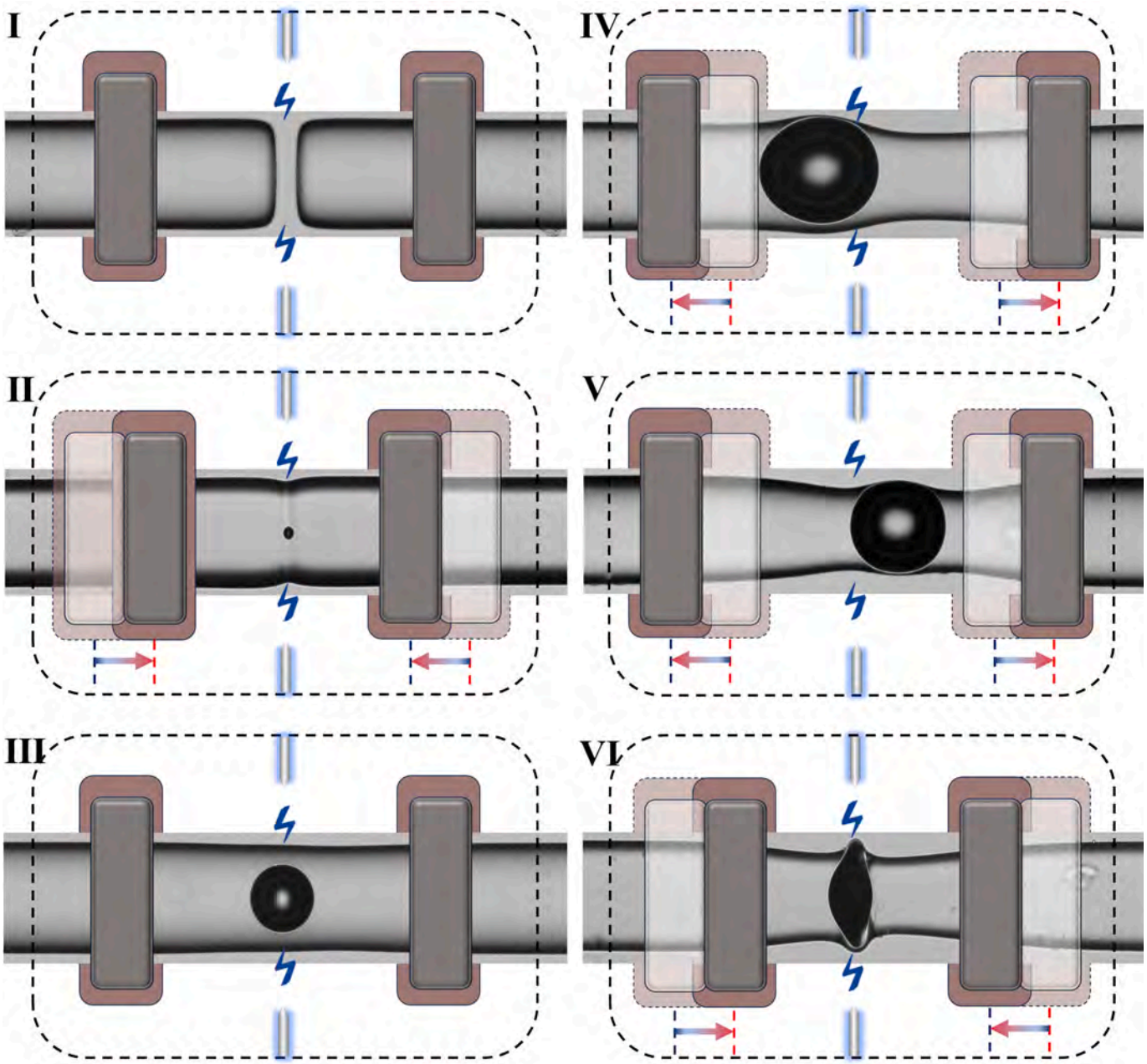

Fig. 2. Schematic of the spindle-shaped bubble fabrication process by adaptive fiber micro-shaping.

with a cavity length L_{minor} of 51 μm and a maximum cladding-protruding length D_m of 130 μm, thus yielding a height difference Δh of 35.5 μm. The average minimum residual cladding thickness t_{avg} is about 3.5 μm and significantly larger than those of previously reported bubble-based sensors [13,27], consequently ensuring better resistance to strain and bending. Fig. 3(b) shows the sensor bent around a 5 cm-diameter ring. When the chord length is 565 μm, the vertical displacement d_{bend} reaches 7.2 μm. Based on the geometric relationship between chord length and sagitta (d_{bend}), the local bending radius of the microcavity is calculated as 0.57 cm. This value differs from the macro-scale ring radius due to the distinction between localized microcavity deformation and global bending of the fiber.

The sensor was tested using a reflective demodulation system comprising a Supercontinuum (SC) source, optical circulator, and Optical Spectrum Analyzer (OSA), as shown in Fig. 4(a). Repeated axial strain measurements ($n = 10$) demonstrated a high sensitivity of 49.65 ± 0.28 pm/με (mean ± Standard Deviation, SD) (Fig. 4b). The sensor-maintained linearity ($R^2 > 0.995$) within 0–480 με, as spectral overlap occurred beyond this range, while exhibiting exceptional repeatability (Relative Standard Deviation, RSD = 0.57 %), confirming design reliability. The inset reveals a FSR of 24.2 nm at 0 με, corresponding to a theoretical cavity length $L_{minor} = 49.64$ μm, consistent with microscopic measurements.

Temperature testing across 23.5–391.6 °C (Fig. 4c) exhibits an ultralow sensitivity of 0.825 ± 0.014 pm/°C (mean ± SD, $n = 5$, RSD = 1.70 %), reducing strain-temperature cross-sensitivity to 0.016 με/°C. This performance, coupled with zero hysteresis in cyclic loading tests, positions the sensor as a robust solution for applications demanding both precision and thermal stability, such as aerospace structural health monitoring or biomedical wearable devices.

Sensor repeatability was validated by comparing strain sensitivities during ascending (0 → 960 με) and descending (960 → 0 με) loading cycles, as shown in Fig. 5(a). Axial strain was applied using a precision translation stage at 160 με increments with 5-minute intervals, while

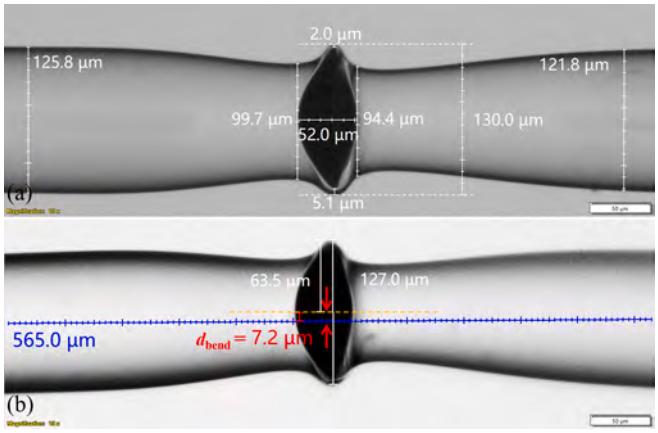

Fig. 3. Microscope images of the device: (a) Straight/unstrained and (b) Bent optical fiber sensor.

spectral responses were recorded (inset, Fig. 5a). Linear regression analysis revealed strain sensitivities of 47.34 pm/με (loading) and 46.93 pm/με (unloading), demonstrating excellent repeatability with minimal deviation (<1%). Long-term stability was further verified by cyclic tensile testing (Fig. 5b), with a maximum spectral drift of 80 pm observed (inset of Fig. 5b). The reasons for this include slight slippage of the fibers in the fixture during long-term loading (resulting in a slight decrease in sensitivity) and unavoidable vibrations of the 3D translation stage and motor drive mechanism.

3. Results and Discussion

To elucidate the mechanism of the strain sensitivity enhancement, four bubble-microcavity FPIs are fabricated, and the parameters are shown in Fig. 6(a) (S1, S2) and Fig. 6(b) (S3, S4). The strain response is determined using the setup shown in Fig. 4(a), with FSRs measured near 1,550 nm as 9.84 nm, 10.24 nm, 11.88 nm, and 17.2 nm for S1–S4, respectively (Fig. 6c and 6d). Equation (2) is used to validate the accuracy of the microscopic measurements. Numerical fitting reveals strain sensitivities of 10.91 pm/με (S1) and 15.7 pm/με (S2). Microscopy shows similar t_{avg} and L_{minor} for both, but S2 shows a significantly larger Δh (Fig. 6a), thus confirming that the cladding-protruding structures improve the sensitivity. The strain sensitivities of S3 and S4 are 13.14 pm/με and 19.53 pm/με, respectively. The microscopic images show that S3 and S4 have similar t_{avg} and Δh. The significant difference lies in that L_{minor} of S4 is much smaller than that of S3. All in all, the experimental results show that a smaller length of the bubble microcavity gives rise to greater strain sensitivity.

As shown in Fig. 7, numerical models of S1–S4 under 1,000 με strain are established using COMSOL Multiphysics to investigate the sensitivity enhancement mechanism of the spindle-shaped bubbles [28]. All the models have the same parameters except the geometry, with a uniform average wall thickness t_{avg} = 3.5 μm. For the elliptical bubble (S1), stress and deformation concentrate in the thinnest wall regions ($\sigma_{\varepsilon,\ max}$ = 1.04 GPa, $u_{\varepsilon,\ max}$ = 0.713 %) to form localized strain distributions (Fig. 7a1 and 7b1). Comparative analysis reveals that increasing Δh (S2) boosts the free-end displacement Δd by over 100 % (from 0.467 μm to 0.938 μm) under the same axial strain. This phenomenon arises from the cantilever effect, in which the spindle-shaped structure converts axial strain into long-axis bending deformation and amplifies the cavity-length modulation ΔL by mechanical leverage. Notably, the strain distribution in S2 extends from the localized zones to the root of the protruding region (Fig. 7a2 and 7b2), thereby reducing $u_{\varepsilon,\ max}$ to 0.556 % (22 % lower than S1). The comprehensive performance factor F increases from 1.21 (S1) to 2.25 (S2), showing an improvement of 86 % and confirming that a larger Δh enhances both the sensitivity and tensile resistance through optimized deformation conversion. Simulations of S3 and S4 demonstrate that reducing L_{minor} from 99.6 μm (S3) to 71.8 μm (S4) increases the compressive strain at the long-axis tip by 68.9 % while

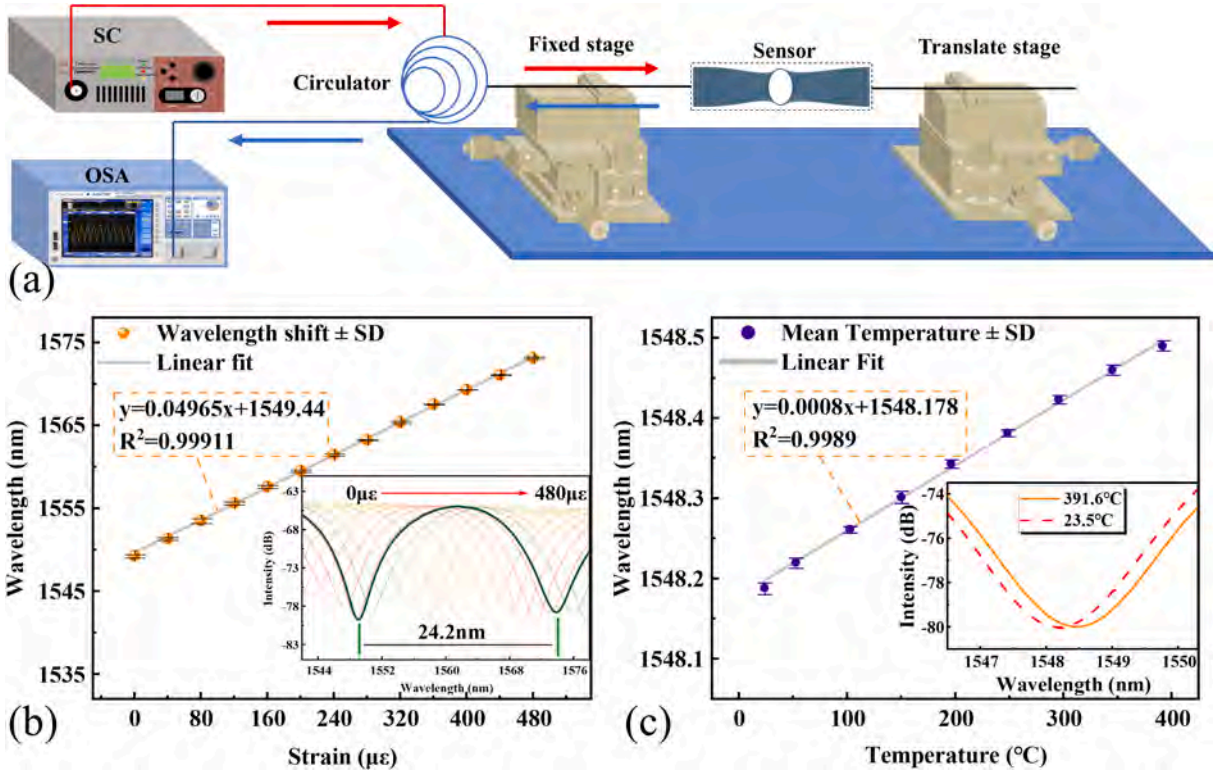

Fig. 4. (a) Schematic of the strain-sensing experimental setup; (b) Strain response of the sensor (*inset*: reflection spectra under different strains); (c) Temperature response of the sensor (*inset*: reflection spectra under different temperatures).

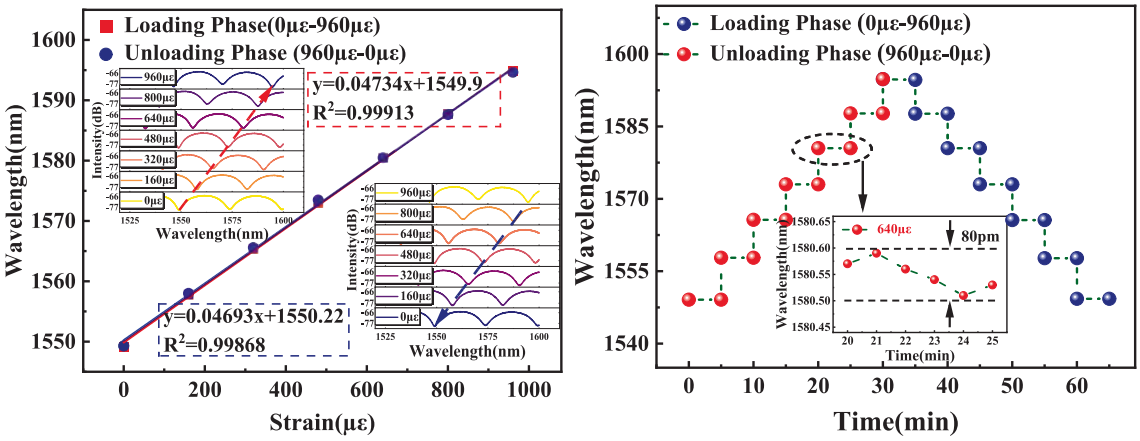

Fig. 5. (a) Strain response during loading (red, 0 → 960 με) and unloading (blue, 960 → 0 με) cycles. Solid lines: linear fits. (b) The stability test results of the proposed sensor. (For interpretation of the references to colour in this figure legend, the reader is referred to the web version of this article.)

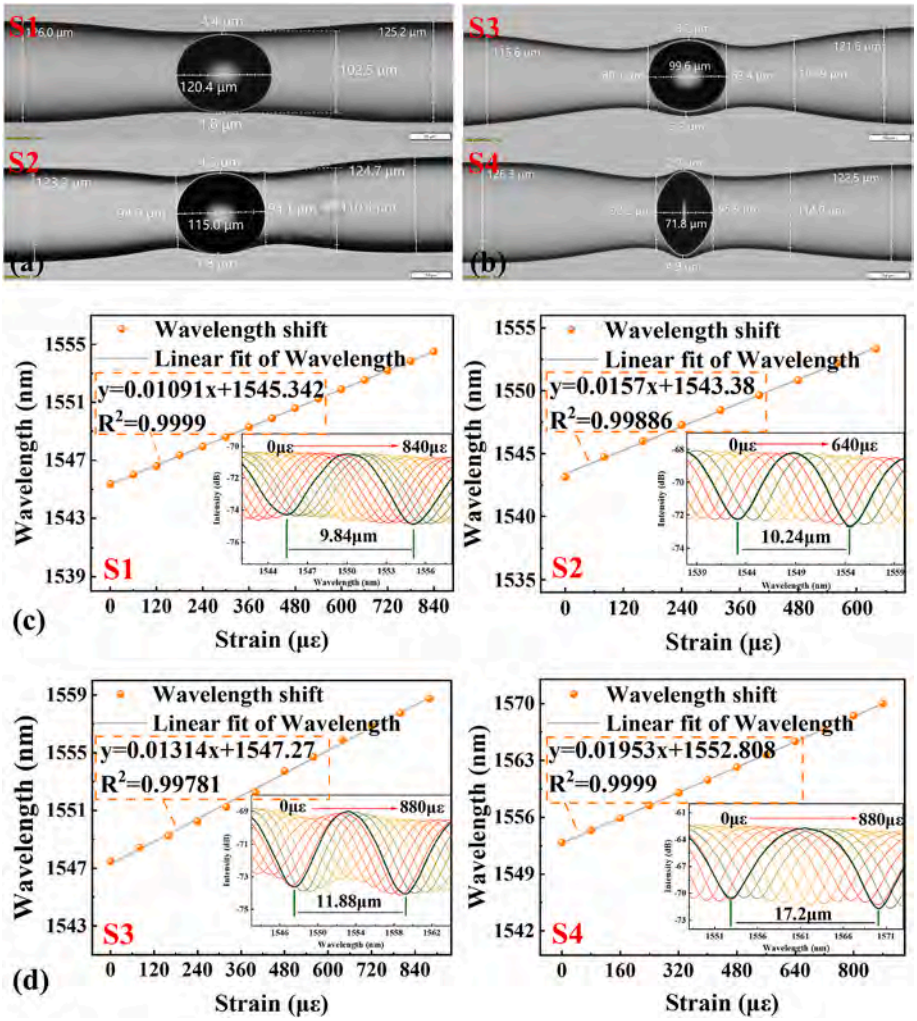

Fig. 6. Microscopic images of four bubble-microcavity FPIs: (a) S1 and S2 with similar t_{avg} and L_{minor}; (b) S3 and S4 with similar t_{avg} and Δh; (c) and (d) Fitted strain-wavelength shift curves of the corresponding sensors (*insets*: reflection spectra).

significantly lowering the cantilever bending stiffness to amplify free-end deformation (Fig. 7b4). Specifically, Δd is 1.94 μm (100 % higher than S3), ΔL is 1.8 μm (+38.5 %), and $u_{\varepsilon,\ max}$ is 1.4 % (+170 %). Quantitatively, the performance factor $F = 2.51$ is nearly double that of F of 1.29, indicating that shortening L_{minor} boosts the sensitivity at the expense of structural durability (local strain surges) and deformation efficiency.

As shown in Fig. 8, numerical models of S1–S4 under bending (radius = 2.5 cm) are established to evaluate the impact of key structural parameters on the bending tolerance. For the elliptical bubble (S1),

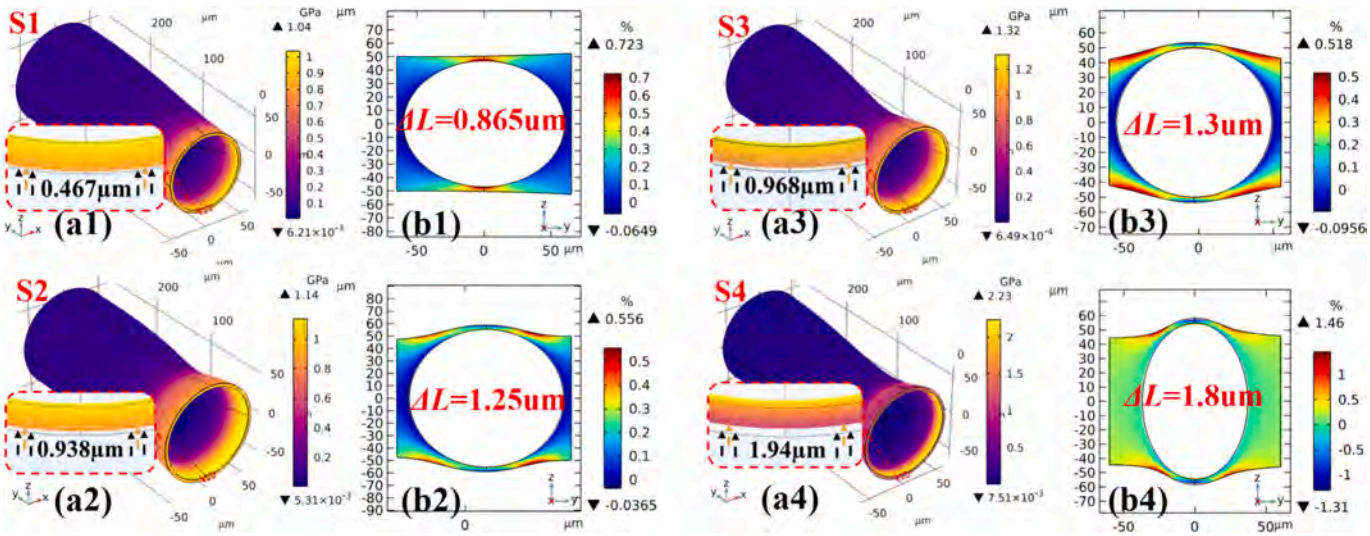

Fig. 7. Three-dimensional stress distributions (a1–a4) and axial cross-sectional strain distributions (b1–b4) of the four bubble-microcavity FPIs. The numerical model of the fiber has a total length of 10 cm, subjected to an axial tensile strain of 1,000 με. Silica parameters used in the simulations: Young's modulus $E = 70$ GPa, Poisson's ratio $\nu = 0.17$, and Density $\rho = 2{,}200$ kg/m^3.

strain remains localized, but the maximum compressive strain at the inner bending side (0.789 %) exceeds the tensile strain (0.597 %) (Fig. 8a). Comparative analysis reveals that increasing Δh (S2) slightly enhances the cavity offset (d_{bend} from 2.925 μm to 3.2 μm), a phenomenon attributed to the cantilever effect in which the original localized strain disperses across a broader area to enable larger macroscopic bending-induced displacement (d_{bend}) while reducing the maximum local strain to 0.615 % (22 % lower than S1). The results confirm that increasing Δh improves the bending tolerance, while simultaneously exposing a critical flaw in traditional elliptical cavities – The localized strain concentration and high compressive strain synergistically increase the bending sensitivity, consequently limiting their applicability under large deformations.

Simulations of S3 and S4 demonstrate that a shorter L_{minor} boosts the strain sensitivity at the expense of bending tolerance. Specifically, S4 exhibits a maximum local strain $u_{\theta,\,max} = 1.47$ % (131 % higher than S3) due to reduced cantilever bending stiffness, thus concentrating deformation in the cladding-protruding region (Fig. 8d). This highlights the following trade-off: shortening L_{minor} enhances sensitivity but degrades the bending resistance. Notably, S3 exhibits a unique strain distribution under bending, and the compressive strain at the inner cavity side (0.434 %) is lower than the tensile strain (0.635 %), likely linked to the smaller average cladding diameter (D_{avg}).

As shown in Fig. 9(a), three microcavity models (**I**: elliptical; **II**: rectangular; **III**: spindle-shaped) with identical L_{minor} are formed to quantify the effects of geometry and wall thickness on the sensitivity, tensile resistance, and bending tolerance. Models **I** and **II** comprise the same tapered cladding structure, while Model **III** adopts the cladding geometry from the sensor in Fig. 3. The key findings in Fig. 9(b–d) include:

(1) For the different types, thinner walls yield higher sensitivity, with the spindle-shaped design (Model **III**) outperforming others for the same t_{avg}. For $t_{avg} = 3.5$ μm, Model III shows $\Delta L = 3.93$ μm (6.2 × Model **I**, 4.1 × Model **II**) and $F = 0.92$ (1.93 × Model **I**, 1.1 × Model **II**).

(2) For the same sensitivity, Model **III** exhibits superior mechanical robustness, and compared to Model II ($t_{avg} = 0.5$ μm), Model III ($t_{avg} = 4$ μm) shows 49.4 % higher F, 32.1 % lower $u_{\varepsilon,\,max}$, and 36.2 % lower $u_{\theta,\,max}$.

(3) The spindle geometry exhibits peak deformation efficiency, and for $t_{avg} = 3.5$ μm, Model **III** achieves 52.1 % higher F, 19.6 % larger ΔL, 21.4 % lower $u_{\varepsilon,\,max}$, and 29 % lower $u_{\theta,\,max}$ than Model **II** ($t_{avg} = 0.5$ μm).

The detailed comparison is summarized in Table 1.

4. Conclusion

The spindle-shaped bubble microcavity fiber sensor described here overcomes the Fully-embedded trade-off between sensitivity and

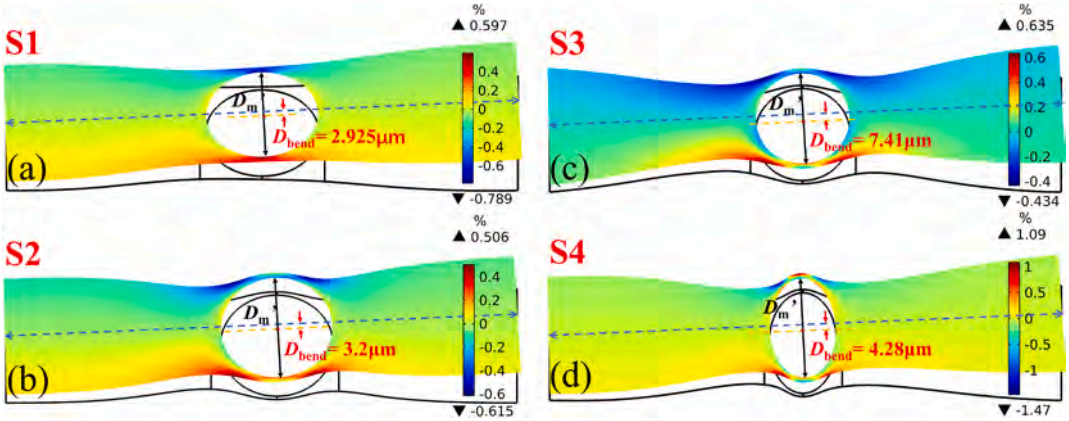

Fig. 8. Cross-sectional deformation distributions of four bubble-microcavity FPIs (S1, S2, S3, S4) under bending around a 5 cm-diameter ring.

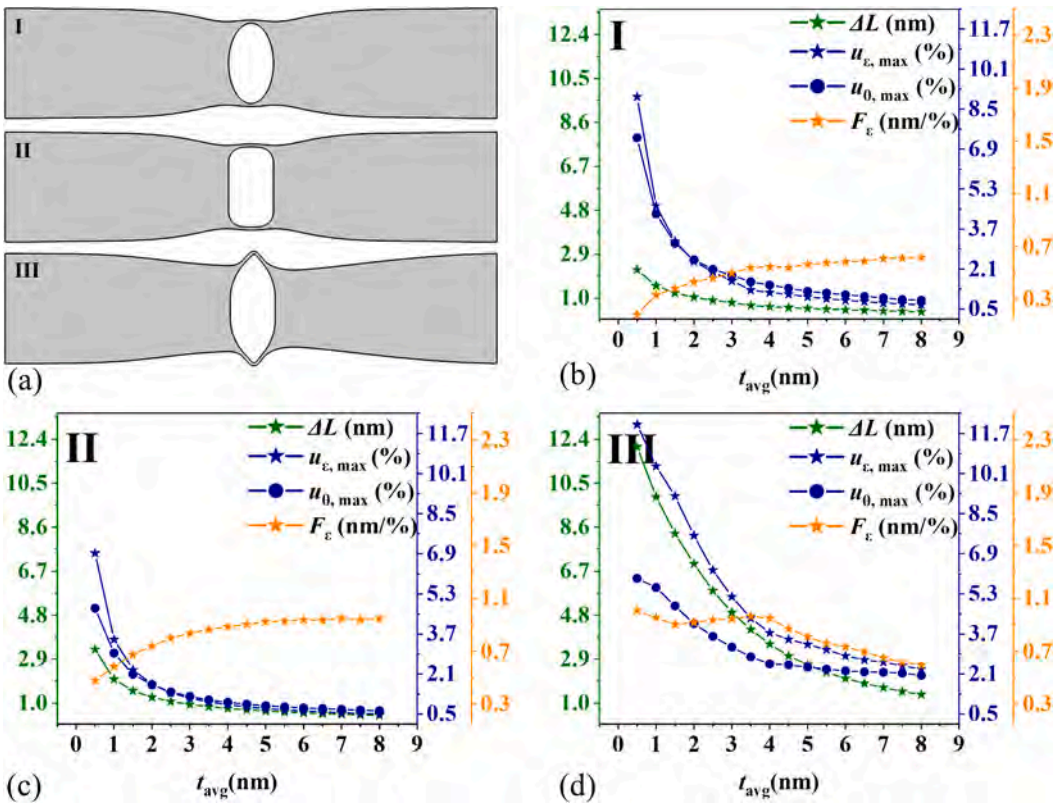

Fig. 9. Numerical simulations of different bubble geometries: (a) Three bubble models with baseline parameters (D_{avg} = 97 μm, L_{minor} = 51 μm): **I** (elliptical, Δh = 1.616 μm), **II** (rectangular, Δh = 1.616 μm), **III** (spindle-shaped, Δh = 33 μm); (b-d) Cavity-length sensitivity (left axis), maximum deformation (right axis 1), and comprehensive performance factor F (right axis 2) for bubbles **I**–**III** with different wall thicknesses.

Table 1
Comparison of different microcavity structures.

Parameters	Elliptical (t_{avg} = 0.5 μm)	Rectangular (t_{avg} = 0.5 μm)	Spindle-shaped (t_{avg} = 3.5 μm)	Spindle-shaped (t_{avg} = 4 μm)	Conclusion
F_ε(μm/%)	**0.183**	**0.635**	**0.966**	**0.949**	Larger cavity-length change (ΔL) under identical deformation, with > 52.1 % improvement in deformation conversion efficiency (F)
ΔL(μm)	**2.228**	**3.497**	**4.1827**	**3.5496**	significantly enhanced ΔL under identical strain, achieving > 19.6 % higher sensitivity
$u_{\varepsilon,\,max}$(%)	**8.99**	**5.51**	**4.33**	**3.74**	>21.4 % reduction in maximum tensile strain ($u_{\varepsilon,\,max}$), indicating superior tensile resistance
$u_{0,\,max}$(%)	**7.35**	**3.92**	**2.78**	**2.5**	>29 % lower maximum bending strain ($u_{0,\,max}$), demonstrating improved bending tolerance

mechanical reliability for optical fiber strain sensors. By engineering a cladding-protruding geometry, the sensor leverages a cantilever-like amplification mechanism to convert axial strain into amplified cavity-length modulation, consequently achieving a high sensitivity of 49.65 pm/με at 1,550 nm. Crucially, this is attained without compromising the structural integrity. The sensor can withstand bending radii as small as 2.5 cm and tensile strain exceeding 1,500 με, consequently outperforming Fully-embedded bubble-based FPIs by 32.1 % in tensile resistance and 36.2 % in bending tolerance. The fabrication process, which utilizes only a commercial fusion splicer and eliminates hazardous chemicals (e.g., HF for etching), ensures both cost-effectiveness and industrial scalability. These advancements position the sensor as an ideal candidate for demanding applications such as flexible electronics and complex wiring systems, where simultaneous requirements for precision, durability, and miniaturization have been challenging to achieve.

CRediT authorship contribution statement

Jianxin Wang: Writing – review & editing, Writing – original draft. **Weiqiang Wang:** Writing – original draft. **Jingwei Lv:** Writing – review & editing, Funding acquisition. **Famei Wang:** Writing – review & editing, Software. **Wei Liu:** Supervision. **Zao Yi:** Writing – review & editing. **Qiang Liu:** Writing – review & editing. **Paul K. Chu:** Writing – review & editing, Funding acquisition. **Chao Liu:** Writing – review & editing, Funding acquisition.

Declaration of competing interest

The authors declare that they have no known competing financial interests or personal relationships that could have appeared to influence the work reported in this paper.

Acknowledgements

The work was jointly supported by the Heilongjiang Provincial Natural Science Foundation of China [JQ2023F001], National Natural Science Foundation of China [12304480], Natural Science Foundation of Heilongjiang Province [LH2021F007], China Postdoctoral Science Foundation funded project [2020 M670881], as well as City University of Hong Kong Donation Research Grants [DON-RMG 9229021 and 9220061].

Data availability

No data was used for the research described in the article.

References

[1] J. Wang, X. Lu, C. Mi, Q. Yin, J. Lv, L. Yang, et al., Ultra-high sensitivity photonic crystal fiber sensor based on dispersion turning point sensitization of surface plasmonic polariton modes for low RI liquid detection, Opt. Express 32 (2024) 32895–32908.
[2] J. Zhao, Y. Zhao, Y. Peng, Z.-T. Lin, X.-G. Hu, Simultaneous measurement of salinity and temperature based on Fabry-Perot interference and anti-resonance effect, Sens. Actuators B 369 (2022) 132248.
[3] W. Liu, Y. Shi, Z. Yi, C. Liu, F.M. Wang, X.L. Li, et al., Surface plasmon resonance chemical sensor composed of a microstructured optical fiber for the detection of an ultra-wide refractive index range and gas-liquid pollutants, Opt. Express 29 (2021) 40734–40747.
[4] X.-X. Wang, Y. Zhao, R.-Q. Lv, H.-K. Zheng, Optic-fiber vector magnetic field sensor utilizing magneto-shape effect of magnetic fluid, Measurement 202 (2022) 111829.
[5] X. Ding, S. Liu, M. Wang, N. Chen, Y. Wang, Highly sensitive magnetic field sensor using magnetic fluid filled dual-core photonic crystal fiber, Opt. Laser Technol. 175 (2024) 110801.
[6] H. Fu, Z. Sheng, W. Gao, Y. Guo, X. Wang, S. Lou, Ultrahigh Sensitivity Surface Plasmon Resonance magnetic Field Sensor based on Side-Core Inscribed Capillary Fiber, IEEE Sens. J. 24 (2024) 31973–31982.
[7] Z. Chen, J. He, X. Xu, J. He, B. Xu, B. Du, et al., High-temperature sensor array based on fiber Bragg gratings fabricated by femtosecond laser point-by-point method, Acta Opt. Sin. 41 (2021) 1306002.
[8] Y. Zhao, S. Liu, J. Luo, Y. Chen, C. Fu, C. Xiong, et al., Torsion, refractive index, and temperature sensors based on an improved helical long period fiber grating, J. Lightwave Technol. 38 (2020) 2504–2510.
[9] M. Cai, H. Chen, R. Shi, H. Li, S. Zhang, S. Jia, et al., Cryogenic temperature sensor based on fiber optic Sagnac interferometer with a panda polarization-maintaining fiber, Opt. Laser Technol. 180 (2025) 111477.
[10] Y. Wu, Y. Zhang, J. Wu, P. Yuan, Temperature-insensitive fiber optic Fabry-Perot interferometer based on special air cavity for transverse load and strain measurements, Opt. Express 25 (2017) 9443–9448.
[11] L. Cai, J. Wang, M. Chen, X. Ai, A high-sensitivity strain sensor based on an unsymmetrical air-microbubble Fabry-Pérot interferometer with an ultrathin wall, Measurement 181 (2021) 109651.
[12] T.T. Gang, R.X. Tong, C. Bian, A novel strain sensor using a fiber taper cascaded with an air bubble based on Fabry–Pérot interferometer, IEEE Sens. J. 21 (2020) 4618–4622.
[13] S. Liu, K. Yang, Y. Wang, J. Qu, C. Liao, J. He, et al., High-sensitivity strain sensor based on in-fiber rectangular air bubble, Sci. Rep. 5 (2015) 7624.
[14] B. Xu, M. Chen, K. Yang, Y. Guo, D. Wang, C.-L. Zhao, Ultra-high sensitivity strain sensor based on biconical fiber with a bulge air-bubble, Opt. Lett. 46 (2021) 1983–1986.
[15] S. Liu, Y. Wang, C. Liao, G. Wang, Z. Li, Q. Wang, et al., High-sensitivity strain sensor based on in-fiber improved Fabry–Perot interferometer, Opt. Lett. 39 (2014) 2121–2124.
[16] C. Yin, Z. Cao, Z. Zhang, T. Shui, R. Wang, J. Wang, et al., Temperature-independent ultrasensitive Fabry–Perot all-fiber strain sensor based on a bubble-expanded microcavity, IEEE Photonics J. 6 (2014) 1–9.
[17] S. Ma, W. He, L. Xu, Z. Li, Wavelength tunable ring cavity erbium-doped fibre laser based on tapered Fabry Perot filter fabricated by hydrofluoric acid corrosion for stretch sensing, Opt. Fiber Technol. 84 (2024) 103772.
[18] C. Monteiro, S. Silva, O. Frazão, Hollow microsphere Fabry–Perot cavity for sensing applications, IEEE Photon. Technol. Lett. 29 (2017) 1229–1232.
[19] Y. Zhao, F. Xia, M.-Q. Chen, R.-J. Tong, Y. Peng, Optical fiber axial contact force sensor based on bubble-expanded Fabry–Pérot interferometer, Sens. Actuators, A 272 (2018) 318–324.
[20] S. Novais, M.S. Ferreira, J.L. Pinto, Lateral load sensing with an optical fiber inline microcavity, IEEE Photon. Technol. Lett. 29 (2017) 1502–1505.
[21] Y. Zeng, X. Li, J. Lv, J. Wang, H. Zou, W. Liu, et al., Cascaded Fabry-Perot interferometric air bubble strain sensor for finger motions, Infrared Phys. Technol. 105988 (2025).
[22] C. Liu, J. Wang, J. Lv, X. Song, W. Liu, Q. Liu, et al., Economical and easily implemented Vernier effect bubble microcavity FPI for strain sensing with extreme low-temperature cross-sensitivity, Infrared Phys. Technol. 105939 (2025).
[23] J. Lv, W. Kong, J. Wang, W. Li, R. Li, L. Li, et al., High-sensitivity strain sensor with air microbubble based on the Vernier effect, Opt. Fiber Technol. 94 (2025) 104295.
[24] E. Li, G.-D. Peng, X. Ding, High spatial resolution fiber-optic Fizeau interferometric strain sensor based on an in-fiber spherical microcavity, Appl. Phys. Lett. 92 (2008) 101117.
[25] X. Zhou, X. Li, S. Li, X. Yan, X. Zhang, F. Wang, et al., A miniature optical fiber Fabry–Perot interferometer temperature sensor based on tellurite glass, Ieee T Instrum Meas 70 (2021) 1–6.
[26] J. Lv, W. Li, J. Wang, X. Lu, Q. Li, Y. Ren, et al., High-sensitivity strain sensor based on an asymmetric tapered air microbubble Fabry-Pérot interferometer with an ultrathin wall, Opt. Express 32 (2024) 19057–19068.
[27] S. Liu, Z. Sun, L. Zhang, C. Fu, Y. Liu, C. Liao, et al., Strain-based tunable optical microresonator with an in-fiber rectangular air bubble, Opt. Lett. 43 (2018) 4077–4080.
[28] J. Wang, W. Liu, Q. Li, W. Li, L. Yang, J. Lv, et al., A high-sensitivity strain sensor based on the core-offset fiber with a micro air bubble, Opt. Commun. 555 (2024) 130235.